

Electrochemical-Thermal-Mechanical Coupling of Lithium-Ion Battery Model in LS-DYNA[®]

Kyoungsu Im¹, Jaeyoung Lim², Kyu-Jin Lee³, Z.-C. Zhang¹, and Grant Cook, Jr.¹

¹Livermore Software Technology, an ANSYS Company, Livermore, CA 94551, USA

²Hyundai Motor Group R&D Division, Gyeonggi-do, 18280, KOREA

³Dept. of Mech. Eng., Myongji University, Yongin 449-728, KOREA

Abstract

In this paper, we report a new development of battery-thermal-structure-interaction (BTSI) based on previously developed electrochemical Lithium-Ion models: i) a single insertion lithium metal model, and ii) a dual insertion composite model. In 10 cells of a lithium ion battery stack, each cell consists of Graphite(LiC₆) anode/Separator/high performance layered LMO(LiMn₂O₄) or NCM(LiNi_{1/3}Co_{1/3}Mn_{1/3}O₂) cathode, which has been strongly proposed as a candidate for automotive batteries because of its high capacity, thermal stability, and low volume change rate (cycle performance). For the thermal-mechanical analysis, each layer in a cell and outside case are modeled corresponding to their material properties. Then, a rigid ball impacts center top position of the cell stack in order to investigate the thermal and mechanical responses of a lithium ion battery stack. To see the cell responses in different state of charge (SOC), we selected the first 20 second of the discharging processes. The results show that after the ball impact the cell stack, then the mechanical deformation started and 6 seconds after the ball compressed, a strong hot spot developed inside cell stack and the temperature increased exponentially over the melting point of the lithium, 453K. Although we demonstrated a simple impact problem to show how to simulate the electrochemical-thermal-mechanical problem, the current solver can be used to solve more practical problems such as a cellular phone drop test, notebook battery impacting test, and even deformation test of the scaled-up electric vehicle(EV) battery pack.

Introduction

The research and technology of lithium-ion batteries (LIB) has grown extensively since Sony first introduced it on the market in 1991. Such a technology nowadays becomes a stand power source in a broad range of indispensable life equipment including cellphones, laptop computers, and electric vehicles (EV). The most comparative advantages of LIB from the conventional batteries include [1]: i) efficient rate and high power discharge capability, ii) distinguished specific energy and its energy density, iii) stable operation with a wide range of temperature, iv) small discharge rate and long life cycle, and so on. Such excellent features now make it possible to replace EV batteries gradually. For example, the Nissan Leaf and most of Tesla Motors's models are widely known commercialized EVs that contain LIBs. Generally, the battery pack in EV are made up of thousands of cells so that it can be possible to accelerate the car from 0 to 60 miles per hour within a few seconds. Furthermore, comparatively long range driving can also be possible with increasing power density of LIB. Although LIB has many excellent features and it has been proven that LIBs are safe enough to the commercial EV, as more energy is stored, more possible dangers for the safety arise. One of the most dangerous and extreme issues with LIB safety is the possibility of thermal runaway [2]. In fact, accidents due to battery malfunctions have been reported. For example, a Tesla model S caught fire started in battery after the EV hit metal debris on a highway [3]. Therefore, it is inevitable that more improvement in the area of the thermal safety is required [2]. In addition, the demand for improvement from thermal degradation in high temperature situations is undeniably required [1].

Chen and Evans [4,5] extended thermal modeling of lithium/polymer battery model to electric vehicle (EV) application using a scaled-up 2D and 3D heat condition model for the serially connected unit cells and parallel connected cell stacks. Without directly calculate the heat generations from LIB models, they used the theoretical capacity equations which fitted by using empirical parameters for discharge and charge processes. The main messages from their simulation shown that the thermal management may not be serious for batteries under low

discharge rate, but in the case of high discharge rate, the temperature will be remarkably increased if the thickness of a cell stack exceed a certain threshold value.

The important attempt at predicting the thermal behavior of the lithium/polymer battery using 1D LIB model was made by Carolyn R. Pals and John Newman [6] who conducted simulations of two different models: a single cell, and a cell stack. In a single cell model, they examined that how cell performance varies with operating temperature for both adiabatic and isothermal discharge. It was shown that cells operating at lower temperature have a lower cell potential and reach their cutoff potential sooner, and at a lower value of active material utilization than cells operating at a higher temperature due to variation with temperature of the salt diffusion coefficient and the ionic conductivity. Using the cell stack model, they demonstrated how the temperature varies in a cell stack depending on thickness and heat transfer conditions and concluded that heat was generated at lower rates in higher temperature areas of the stack, and at higher rates in lower temperature areas of the stack, with such nonuniform heat generation rate make the temperature profiles in the cell stack flatten.

Later on, Song and Evans [7] improved their thermal model for lithium polymer batteries by using electrochemical-thermal modeling. Based on the author's knowledge, this is the first mathematical approach that the electrochemical phenomena is coupled simultaneously with 2D heat conduction. By using Doyle's [8, 9] 1D a single insertion model, they compared to their results to the experimental data for various cell voltages as a function of discharge capacity. Although their results showed some discrepancies, they concluded that their results are in reasonable agreement with the experimental data.

However, there is no model existing for the treatment of the electrochemical-thermal-mechanical (ECTM) phenomena simultaneously. In the present paper, we report the recent development of an ECTM coupled LIB model in LS-DYNA. At a given time step, the heat generation is determined in each structural element that is considered as a 1D electrochemical cell (inside the battery). Based on such heat generations, the thermal solver computes the temperature of cell elements in a 3D computational domain with the electrochemical parameters of each cell. Finally, the thermal solver communicates with mechanical solver by exchanging thermal properties and works done by mechanical solver, which the mechanical properties of the LIB are required and are taken into account, including Yong's modules, stress, and Poisson's ratio [10]. When coupled this way, the mechanical solver transfers its deformation coordinates to the electrochemical LIB solver. It should be noted that the present model is based on the thermodynamics, kinetics, and concentrated solution transport theories in pores of composite electrodes and is intended to assist users in tackling problems ranging from the fundamental battery cell physics to very complex situations such as EV crush models. To this end, we have designed detailed keywords for the electrodes, electrolytes, transport material properties, and even thermal-mechanical couplings for such applications

Modeling of the Lithium Ion Battery

A full understanding of the multi-physics involved in LIB models is necessary for correct simulation of these models. This includes material transport, thermodynamics, and kinetics in the porous electrode. Porous media are normally used with concentrated electrolytes. Such a theory was first pioneered by Newman and Tiedman [11]. In their porous electrode theory, the properties determining the battery performance were averaged over a small volume in all dimensions of the electrode without specifying the exact positions, shapes of all electrode particles, and the exact pores in each electrode. Thus, the porous electrode is considered as the superposition of all materials coexisting in the active insertion material, filler, and electrolyte at every point of the geometry. In what follows, we will first review and construct the transport model equations based on the concentrated solution theory, the potential equations with thermodynamics, equations for electrochemical kinetics and the current balance, and then, the energy balance equations including heat generation in a single cell and scaled-up energy equation.

Transport

The driving force acts on species i , and causes it to move with respect to the surrounding fluid. This is determined by the difference of the electrochemical potential multiplied by species concentration, which is in turn given as the Stefan-Maxwell multicomponent diffusion equation [12,13]:

$$c_i \nabla \mu_i = \sum_j K_{ij} (\mathbf{v}_j - \mathbf{v}_i) = RT \sum_j \frac{c_i c_j}{c_T D_{ij}} (\mathbf{v}_j - \mathbf{v}_i) \quad (1)$$

where μ_i is the electrochemical potential of species i , K_{ij} are friction coefficients, and \mathbf{v}_i is the velocity of species i . With the selection of a reference velocity, which is chosen for the solvent, these equations can be inverted to yield flux equations for the anion and cation in a binary electrolyte,

$$c_+ \nabla \mu_+ = K_{0+} (\mathbf{v}_0 - \mathbf{v}_+) + K_{+-} (\mathbf{v}_- - \mathbf{v}_+) \quad (2a)$$

$$c_- \nabla \mu_- = K_{0-} (\mathbf{v}_0 - \mathbf{v}_-) + K_{-+} (\mathbf{v}_+ - \mathbf{v}_-) \quad (2b)$$

since the flux density of species i is given by

$$N_i = c_i \mathbf{v}_i \quad (3)$$

and the current density in an electrolyte solution given by

$$i = F \sum_i z_i N_i \quad (4)$$

Then, the equation can be rearranged as,

$$N_+ = c_+ \mathbf{v}_+ = -\frac{v_+ D c_T}{v R T c_0} c \nabla \mu_e + \frac{i_2 t_+^0}{z_+ F} + c_+ \mathbf{v}_0 \quad (5a)$$

$$N_- = c_- \mathbf{v}_- = -\frac{v_- D c_T}{v R T c_0} c \nabla \mu_e + \frac{i_2 t_-^0}{z_- F} + c_- \mathbf{v}_0 \quad (5b)$$

where $c = c_+ / v_+ = c_- / v_-$, $v = v_+ + v_-$, and $\mu_e = v_+ \mu_+ + v_- \mu_- = \mu_e^0 + v R T \ln(\gamma_{\pm} m)$, with $m = c / c_0 M_0$. The diffusion coefficient of electrolyte and the transference number with respect to the solvent are related to the diffusion coefficients by

$$D = \frac{D_+ D_- (z_+ - z_-)}{z_+ D_{0+} - z_- D_{0-}}, \quad (6)$$

and

$$t_+^0 = 1 - t_-^0 = \frac{z_+ D_{0+}}{z_+ D_{0+} - z_- D_{0-}} \quad (7)$$

From porous electrode theory, a differential material balance can be averaged over the volume of the pores in an element of the electrode, and the surface integrals can be introduced by means of the divergence theorem and the final mass balance for species i [14]:

$$\varepsilon \frac{\partial c_i}{\partial t} = -\nabla \cdot \mathbf{N}_i + a j_{in} \quad (8)$$

where c_i is an average over the volume of the solution in the pores, j_{in} is an average over the interfacial area between the matrix and the pore solution, and N_i is an average over a cross section through the electrode, cutting matrix and pore. It should note that three different averages are applied to derive the mass transport, Eq.(8) in porous media.

The diffusion coefficient of the salt which is the property commonly measured for a binary electrolyte can be related to the diffusion coefficient of the electrolyte by,

$$D = D \frac{c_T}{c_0} \left(1 + \frac{d \ln \gamma_{\pm}}{d \ln m} \right) \quad (9)$$

where γ_{\pm} is the mean molal activity coefficient and m is the molality. The gradient of chemical potential can be expressed in terms of the gradient of concentration:

$$\frac{D}{vRT} \frac{c_T}{c_0} c \nabla \mu_e = D \left(1 - \frac{d \ln c_0}{d \ln c} \right) \nabla c \quad (10)$$

Using the above relation, the flux of species i can be expressed as,

$$N_i = -v_i \left(1 - \frac{d \ln c_0}{d \ln c} \right) D \nabla c + \frac{i_2 t_i^0}{z_i F} + c_i v_0 \quad (11)$$

Detailed derivation of Eq. (10) (or from Eq. (5) to Eq. (11)) can be found in Appendix A[15]. Finally, by inserting equation (11) into equation (8), the mass transfer equation in porous media can be derived as,

$$\varepsilon \frac{\partial c}{\partial t} + \nabla \cdot (c v_0) = \nabla \cdot \left[\varepsilon D \left(1 - \frac{d \ln c_0}{d \ln c} \right) \nabla c - \frac{\nabla \cdot (i_2 t_+^0)}{z_+ v_+ F} \right] + a j_+ \quad (12)$$

Convection in the electrolyte is usually negligible and $z_+ v_+$ is 1 for most salts used in LIBs. The boundary condition on the salt concentration at a lithium foil electrode (a single insertion model) is found by setting the anion flux to zero:

$$\varepsilon \frac{\partial c}{\partial x} \Big|_{x=0} = - \frac{I(1-t_+^0)}{FD} \quad (13)$$

At the boundary between the positive electrode and current collector, the flux of ions is equal to zero, and all of the current is carried by electrons, so the salt concentration and the current density of electrolytes is set to zero:

$$\nabla c = 0 \text{ and } \mathbf{i}_2 = 0, \text{ at } x=XL \quad (14)$$

For the dual insertion model, the boundary conditions on negative electrode and current collector are analogous to those of the positive case. The porous solid phase in most LIBs contains particles which can be modeled as spheres. If volume changes in the solid are negligible, the mass balance reduces to,

$$\frac{\partial c_s}{\partial t} = \frac{1}{r^2} \frac{\partial}{\partial r} \left(D_s r^2 \frac{\partial c_s}{\partial r} \right) \quad (15a)$$

with the boundary conditions,

$$\frac{\partial c}{\partial r} \Big|_{r=0} = 0, \text{ and } -D_s \frac{\partial c}{\partial r} \Big|_{r=R} = j_{Li^+} \quad (15b)$$

and initial condition,

$$c_s(t=0, r) = c_s^0 \quad (15c)$$

The second boundary condition is constructed by relating the pore wall flux across the interface with the rate of transport of lithium ions into the solid phase. Under the diffusion process, the superficial area per unit volume of the porous electrode is related to the particle radius:

$$a = \frac{3(1-\varepsilon)}{R_s} \quad (16)$$

Potential

In LIB model, the gradient of the potential in the solution is to be defined with respect to a lithium reference electrode in solution [14]:

$$\nabla \Phi_2 = - \frac{i_2}{\kappa} + \frac{RT}{F} (1-t_+^0) \cdot \left(1 + \frac{d \ln f_A}{d \ln c} \right) \nabla \ln c \quad (17)$$

The second term on the righthand side accounts for concentration overpotential. In porous media, the conductivity is corrected by the Bruggeman relation, $\kappa = \varepsilon^{1.5} \kappa_\infty$ where κ_∞ is the conductivity of the bulk electrolyte. Since only potential differences, and not absolute potentials, are measurable, the potential in the solution has an arbitrary datum as a boundary condition. Here, we set $\Phi_2 = 0$ at the positive electrode-current collector interface.

The potential in the porous electrode is determined from Ohm's Law,

$$\nabla \Phi_1 = - \frac{i_1}{\sigma} = - \frac{(I - i_2)}{\sigma} \quad (18)$$

Where $i_1 = I - i_2$ is the current in the electrode phase and the electronic conductivity of the bulk solid is corrected for the volume fraction of the electrode by the Bruggeman relation, $\sigma = \sigma_\infty (1 - \varepsilon)$, where σ_∞ is the conductivity of the nonporous composite electrode. Note that there is only one boundary condition in each electrode region. For galvanostatic operation, the boundary condition in the negative electrode is $i_2 = I$ at the negative electrode-separator interface, and in the positive electrode it is $i_2 = 0$ at the positive electrode-current collector interface.

Reaction Rate

The simplest type of dependence of the current density on the surface overpotential and composition adjacent to the electrode surface is given by Butler-Volmer equation:

$$i_n = i_0 \left[\exp\left(\frac{\alpha_a F (\Phi_1 - \Phi_2 - U)}{RT}\right) - \exp\left(\frac{\alpha_c F (\Phi_1 - \Phi_2 - U)}{RT}\right) \right] \quad (19)$$

Here, $\eta = \Phi_1 - \Phi_2 - U$ is the surface overpotential, which is a driving force for an electrochemical reaction to occur. U is the open-circuit potential of the solid material evaluated at the surface concentration of the solid with respect to a hypothetical lithium reference electrode in solution just outside the diffuse part of the double layer, at the same local electrolyte concentration, and in general it is a function of solid concentration and temperature in insertion electrodes. Note that U must be specified as a function of intercalant concentration but not as a function of electrolyte concentration.

The magnitude and dependence of U on solid concentration vary considerably among different insertion materials. The shape of the open-circuit potential profile has a large effect upon the simulation results, and accurate data for this property measured with respect to a lithium reference electrode are very important, especially when one is comparing full-cell-sandwich simulations with experimental data. The anodic and cathodic transfer coefficients, α_a and α_c correspond to the fractions of the applied potential which favor the anodic and cathodic directions of the overall reaction, respectively. The exchange current density, i_0 depends on the composition of the solution adjacent to the electrode and the temperature of the electrode surface. The reaction mechanisms at electrode interfaces, particularly in the presence of the solid electrolyte interphase, are not understood in great detail. Fortunately, the rapid kinetics of electrodes used in lithium batteries reduces the importance of the exact reaction mechanism in the battery model. In the absence of more detailed information about reaction mechanisms, Butler-Volmer equation is a good approximation without comparable errors.

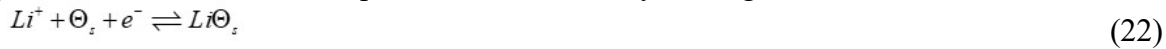
For the common polymer electrolyte, there is experimental evidence for a charge transfer process.



Θ_p represents a site in the polymer lattice. This corresponds to an equilibrium between occupied and unoccupied lithium sites in the solid polymer electrolyte. In this case the exchange current density is defined as,

$$i_0 = F (k_a)^{\alpha_c} (k_c)^{\alpha_a} (c_{\max} - c)^{\alpha_c} (c)^{\alpha_a} \quad (21)$$

A general lithium ion insertion process is described by a charge transfer reaction,



Here, Θ_s represents a site in the solid lattice. For example, at lithium insertion in the lithium manganese oxide spinel, the corresponding reaction is given as,



In addition, the exchange current density is given by,

$$i_0 = F (k_a)^{\alpha_c} (k_c)^{\alpha_a} (c_{s,\max} - c_s)^{\alpha_c} (c_s)^{\alpha_a} (c)^{\alpha_c} \quad (24)$$

Note that the exchange-current density tends to zero as the solid concentration approaches either 0 or $c_{s,\max}$. and since the reaction-rate equation is algebraic, it requires no boundary condition.

Current Balance

The superficial current density i_2 in the pore phase is given by,

$$i_2 = F \sum_i z_i N_i \quad (25)$$

By taking the divergence of the superficial current density, we have,

$$\nabla \cdot i_2 = F \sum_i z_i \nabla \cdot N_i \quad (26)$$

By rearranging Eq. (8) and inserting it into the above equation along with considering the electroneutrality, $\sum_i z_i c_i = 0$, we obtain the divergence of the superficial current density in the solution.

$$\nabla \cdot i_2 = aF \sum_i z_i j_{in} = a i_n \quad (27)$$

where i_n is the average transfer current density and $\nabla \cdot i_2$ is the transfer current per unit volume of the electrode. A single electrode reaction can be written in symbolic form as,



where M_i is a symbol representing the chemical formula of species i and s_i is the stoichiometric coefficient of species i . From Faraday's law, the rate of electrochemical reaction is given by

$$aj_{i,n} = -\frac{as_i}{nF} i_n = -\frac{s_i}{nF} \nabla \cdot i_2 \quad (29)$$

The specific interfacial area a is the surface area of the pore walls per unit volume of the total electrode and thus, $aj_{i,n}$ represents the rate of transfer of the species from the solid phase to the pore solution. Note that because of the electroneutrality, the divergence of the total current density is zero and can be expressed by,

$$\nabla \cdot i_1 + \nabla \cdot i_2 = 0 \quad (30)$$

By rearranging Eq. (15) and inserting into Eq. (22) in above, we can obtain the potential equation in the solution.

$$\nabla \cdot i_2 = \nabla \cdot (\kappa \nabla \Phi_2) + \nabla \cdot (\kappa_D \nabla \ln c) = -aFj_{i,n} \quad (31a)$$

where the diffusional conductivity is given by,

$$\kappa_D = \kappa \frac{RT}{F} (1 - t_+^0) \left(1 + \frac{d \ln f_A}{d \ln c} \right) \quad (31b)$$

Considering Eq. (18) and by applying equation (30), the potential equation in the electrode can be expressed as,

$$\nabla \cdot i_1 = \nabla \cdot (\sigma \nabla \Phi_1) = -\nabla \cdot i_2 = aFj_{i,n} \quad (32)$$

Energy Balance

A single cell in most LIB packs used in industry currently is very thin, less than 300 μ m, so the temperature gradients perpendicular to the electrodes are negligible, considering only the Joule and Peltier heating. Therefore, the heat generation in a 1D model assumes uniform temperature in an individual cell. Once the heat generation in each cell is calculated, it can be inserted into a standard heat transfer equation for the battery geometry, to calculate temperature changes across a tall cell or battery stack. Such models are generally concerned with temperature gradients in two- or three-dimensions. The calculation of the heat generated by a cell and the temperature changes in a cell stack requires an energy balance in a cell. Here, we revisit the energy balance equations in Rao and Newman [16], which presents a form of Bernardi et al.'s energy balance. Considering a single cell and from the first law of thermodynamics,

$$\frac{dH_{tot}}{dt} = \dot{Q} - IV \quad (33)$$

where H_{tot} is the sum of the enthalpy of the species, Q the rate of heat transfer with the surrounding, and IV is the electrical work. The average form of total enthalpy over a small volume element of the cell is given by,

$$\frac{dH_{tot}}{dt} = \frac{d}{dt} \int_v \sum_j \sum_i \varepsilon_j \langle c_{i,j} \rangle \bar{H}_{i,j}^{ref} \quad (34)$$

Here, $\langle c_{i,j} \rangle$ is the concentration of species i averaged locally over phase j , in the way that $\varepsilon \langle c_{i,j} \rangle$ is a superficial concentration. $\bar{H}_{i,j}^{ref}$ refers to the average enthalpy at a reference concentration. Differentiation of the product in the integral in the above equation:

$$\frac{dH_{tot}}{dt} = \int_V \sum_j \sum_i \left[\frac{\partial \varepsilon_j \langle c_{i,j} \rangle}{\partial t} \bar{H}_{i,j}^{ref} + \varepsilon_j \langle c_{i,j} \rangle \frac{\partial \bar{H}_{i,j}^{ref}}{\partial T} \cdot \frac{\partial T}{\partial t} \right] dv \quad (35)$$

Here, it can be identified the heat capacity of the system as,

$$C_p = \int_V \sum_j \sum_i \varepsilon_j \langle c_{i,j} \rangle \bar{C}_{p,i,j}^{ref} dv \quad (36)$$

and ignoring the heat of mixing by flux term, but considering only the rate of transfer of the species, $aj_{i,n}$,

$$\frac{dH_{tot}}{dt} = C_p \cdot \frac{dT}{dt} + \int_V \sum_j \sum_i aj_{i,n} \bar{H}_{i,j}^{ref} dv \quad (37)$$

Considering Faraday's law,

$$aj_{i,n} = - \sum_l \frac{S_{i,l}}{n_l F} ai_{n,l} \quad (38)$$

Then, Eq. (37) becomes,

$$\frac{dH_{tot}}{dt} = C_p \cdot \frac{dT}{dt} - \sum_l \int_V \sum_j \sum_i \frac{S_{i,l}}{n_l F} ai_{n,l} \bar{H}_{i,j}^{ref} dv \quad (39)$$

By introducing the reaction enthalpy change or the enthalpy potential,

$$\Delta H_l = U_{H,l} = - \sum_j \sum_i \frac{S_{i,l}}{n_l F} \bar{H}_{i,j}^{ref} = -T^2 \frac{d}{dT} \left(\frac{U_l}{T} \right) = U_l - T \frac{dU_l}{dT} \quad (40)$$

where U_l is the open circuit potential of reaction l .

By substituting Eq. (40) into Eq. (39), the total enthalpy change becomes,

$$\begin{aligned} \frac{dH_{tot}}{dt} &= C_p \cdot \frac{dT}{dt} + \int_V \sum_l ai_{n,l} U_{H,l} dv \\ &= C_p \cdot \frac{dT}{dt} + \int_V \sum_l ai_{n,l} \left(U_l - T \frac{dU_l}{dT} \right) dv \end{aligned} \quad (41)$$

Finally, if we insert Eq. (41) into Eq. (33), we can have the energy balance relating the heat generation.

$$C_p \cdot \frac{dT}{dt} - \dot{Q} = - \int_V \sum_l ai_{n,l} \left(U_l - T \frac{dU_l}{dT} \right) dv - IV \quad (42)$$

Note that we ignored here the concentration dependence of the heating, which is in general small compared to the other heating mechanisms.

Alternatively, in contrast to the thermodynamic approach, the energy balance can be derived by a local heat generation method. Let the left interface between the anode and current collector lie at $x=0$, and extend to $x=x_1$, the separator extend from $x=x_1$ to $x=x_2$, and the composite cathode from $x=x_2$ to $x=x_3$. The heat generation at an interface consists of two contributions: reversible and irreversible.

$$-\dot{q} = i(\Pi + \eta) \quad (43)$$

where Π is Peltier coefficient and η is the overpotential between the electrode and electrolyte. Detailed derivation of the interface heat generation can be found in Appendix B [15]. The reversible heat, $i\Pi$ is the sum of the corresponding anode and cathode for a whole reaction. So, if the temperature is the same for the anode and the cathode, this reversible heat generation rate is reduced to the usual thermodynamic heat effect, i.e. the entropy change rate for the cell, TdS/dt .

The irreversible heat generation rate due to electrochemical reaction at the composite anode and cathode are,

$$-\bar{q}_a^n = \int_{x_0}^{x_1} ai_n \eta_a dx \quad (44a)$$

$$-\bar{q}_c^n = \int_{x_2}^{x_3} ai_n \eta_c dx \quad (44b)$$

The Joule heating rate due to ohmic losses in solid and electrolyte is $-i \cdot \nabla \Phi$. Let the subscript 1 be for the solid and 2 for the electrolyte. The heat generation in an electrolyte is rather complicated when there is a concentration gradient. However, we ignore the thermal effect of any concentration gradient in the electrolyte again. So, the heat generation in the separator is directly linked to the potential difference in the electrolyte between the two faces of the separator.

$$-\dot{q}_s^J = i \Delta \Phi_s, \quad \Delta \Phi_s = \Phi_2(x_1) - \Phi_2(x_2) \quad (45)$$

In the porous electrodes, the heat generation rate in the electrolyte and active matrix are,

$$-\dot{q}_a^J = \int_{x_0}^{x_1} \left(-i_1 \frac{d\Phi_1}{dx} - i_2 \frac{d\Phi_2}{dx} \right) dx \quad (46a)$$

$$-\dot{q}_c^J = \int_{x_2}^{x_3} \left(-i_1 \frac{d\Phi_1}{dx} - i_2 \frac{d\Phi_2}{dx} \right) dx \quad (46b)$$

Therefore, total irreversible heat generation is given by combining all equations.

$$\begin{aligned} -\dot{q} = & i \Delta \Phi_s + \int_{x_0}^{x_1} \left(ai_n \eta_a - i_1 \frac{d\Phi_1}{dx} - i_2 \frac{d\Phi_2}{dx} \right) dx \\ & + \int_{x_2}^{x_3} \left(ai_n \eta_c - i_1 \frac{d\Phi_1}{dx} - i_2 \frac{d\Phi_2}{dx} \right) dx \end{aligned} \quad (47)$$

Now, by applying integration by parts,

$$\begin{aligned} -\dot{q} = & i \left[\Phi_2(x_1) - \Phi_2(x_2) \right] + i \Phi_1 \Big|_{x_0}^{x_1} - i \Phi_2 \Big|_{x_1}^{x_2} - i \Phi_1 \Big|_{x_2}^{x_3} + i \Phi_2 \Big|_{x_2}^{x_3} \\ & + \int_{x_0}^{x_1} \left(ai_n \eta_a + \frac{di_1}{dx} \cdot \Phi_1 + \frac{di_2}{dx} \cdot \Phi_2 \right) dx + \int_{x_2}^{x_3} \left(ai_n \eta_c + \frac{di_1}{dx} \cdot \Phi_1 + \frac{di_2}{dx} \cdot \Phi_2 \right) dx \end{aligned} \quad (48)$$

Here, we used the current boundary conditions for each interface. For example, $i_1=i$ and $i_2=0$ at $x=x_0$. It is assumed that the reference potential at $x=x_0$ is equal to zero, $\Phi_1(x_0)=0$ and thus, the cell potential is $V=\Phi_1(x_3)$. In addition, consider the relation between the normal flux and the divergence of the current as,

$$ai_n = \frac{di_2}{dx} = -\frac{di_1}{dx} \quad (49)$$

Then, the total heat generation becomes,

$$-\dot{q} = \int_{x_0}^{x_1} ai_n (\eta_a - \Phi_1 + \Phi_2) dx + \int_{x_2}^{x_3} ai_n (\eta_c - \Phi_1 + \Phi_2) dx - iV \quad (50)$$

Since,

$$\eta_a = \Phi_1 - \Phi_2 - U_a, \quad \text{and} \quad \eta_c = \Phi_1 - \Phi_2 - U_c$$

and adding the reversible term into the integral, the final form of the heat generation can be expressed as,

$$-\dot{q} = \int_{x_0}^{x_1} ai_n \left(U_a - T \frac{dU_a}{dT} \right) dx + \int_{x_2}^{x_3} ai_n \left(U_c - T \frac{dU_c}{dT} \right) dx - iV \quad (51)$$

Note that the above equation is the same as Eq. (42) if we add inside terms of integration except the unsteady term.

For the scaled-up battery geometry, one can use a standard heat transfer equation to calculate temperature changes across a cell stack or battery pack.

$$\frac{\partial}{\partial t} (\rho c_p T) + \nabla \cdot (\mathbf{v}T) = \nabla \cdot (\lambda \nabla T) + \dot{q} \quad (52)$$

LIB Models

In the previous sections, we described or derived all equations needed for LIB models. It is noted that the mass transports equations are partial differential equations, both the potential equations and the current equation are ordinary differential equations, and the reaction rate, the Butler-Volmer model is an algebraic equation. In case of not needing to explicitly calculate j_{in} and i_2 , the two equations may be combined into one equation.

i) 6 equation model: The first full electrochemical model which was first presented by Doyle, Fuller, and Newman [8,9] can be completed using Eq. (12), (15), (17), (18), (19), and (29) for the 6 unknown variables: c , c_s , Φ_1 , Φ_2 , i_2 , and j .

To describe the electrochemical performance of the cell, the coupled governing equations must be solved simultaneously. It is important to note that since the Butler-Volmer equation makes the system nonlinear, the equation involving it as a source term must be linearized to ensure the convergence.

ii) 4 equation model: Equation (12), (15), (31), and (32) can constitute a complete set of model equations for the first 4 unknown variables in the previous model. After solving all equations either coupled or sequentially, the superficial current density is determined in terms of either potential gradient in the electrode (or electrolyte) phase or the interfacial transfer current density. However, Eq. (31) and (32) must be carefully solved since the source term, Butler-Volmer equation, is strongly nonlinear, indicating that it should be well treated with linearization process before solving the implicit iteration for them.

Results and Discussion

The open circuit potential which sometimes called the equilibrium potential is in general given as a function of the amount of lithium inserted (solid concentration) and and temperature by an experimental data. Fig.1(a) and (b) show the open circuit potential for the graphite, LiC_6 of the anode and LiMn_2O_4 of the cathode.

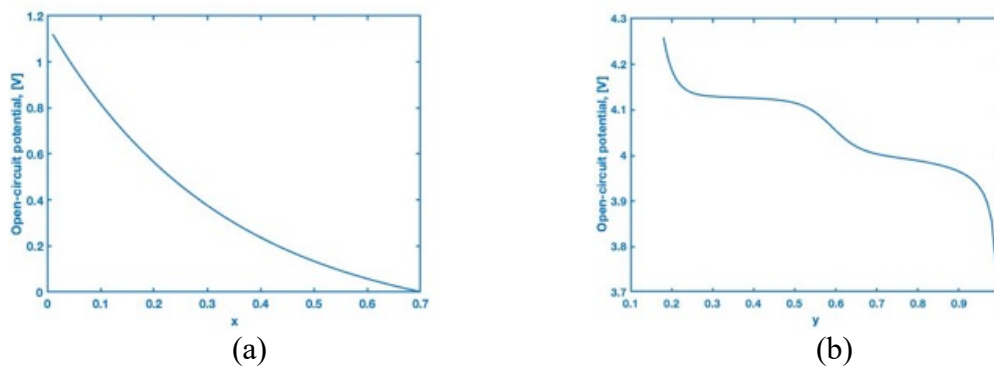


Figure 1 Open circuit potential curves: (a) LiC_6 of the anode, and (b) LiMn_2O_4 of the cathode.

Figure 2(a) shows the problem descriptions of the rigid ball impacting on the cell stack which consists of 10 cells of LIBs. Each cell has the negative current collector ($10\ \mu\text{m}$), anode composite electrode ($100\ \mu\text{m}$), separator ($52\ \mu\text{m}$), cathode composite electrode ($174\ \mu\text{m}$), and positive current collector ($10\ \mu\text{m}$), respectively. Since the cell stack accumulates serially, the total thickness of the cell stack measures $3.46\ \text{mm}$. To protect the LIB stack, the steel case of $1\ \text{mm}$ covers the outside of the battery. Thus, overall dimension of the LIB model in present study has $317\ \text{mm} \times 97\ \text{mm} \times 5.46\ \text{mm}$ as shown in Fig. 2(a). It should be noted that each solver in LS-DYNA can be assigned an independent part to solve in its own region. For example, the electrochemical battery solver can be assigned to solve only part 1~3, which covered all battery parts, while the thermal solver solves all parts except the rigid ball which assigned to the mechanical solver that includes the other parts. In addition, each electrochemical cell has 220 mesh points in the current flowing direction, x-direction. Therefore, one can consider it as a simple battery-thermal-mechanical interacting (BTMI) problem since the battery solver has its own 1D

mesh system in each battery structural elements, and also, the thermal-mechanical solver has its own 3D mesh system.

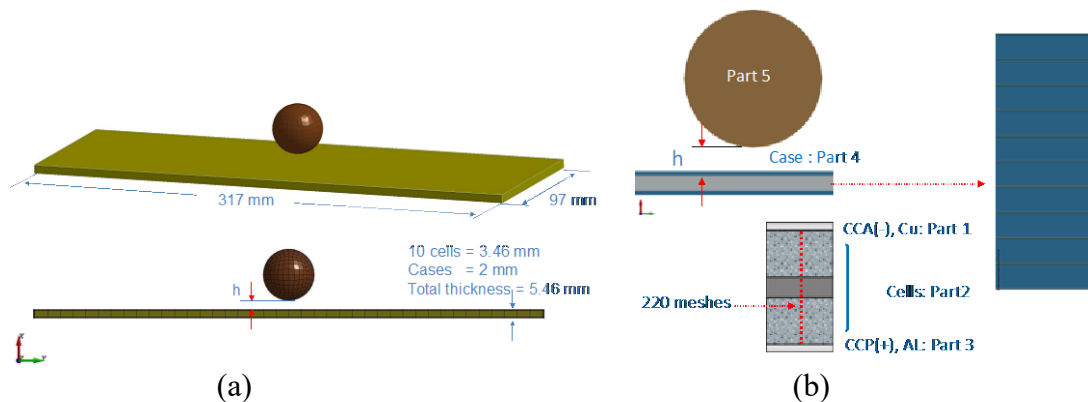


Figure 2 Schematics of the ball impact on the 10 cells of LIB and detailed set up of the problem with corresponding to parts.

Figure 3(b) shows validation curves compared with well-known simulation and experiment data [17] for the discharge capacity as a function of time calculated at different current densities from 1.75 A/m^2 to 35 A/m^2 . Doyle and Newman [17] calculated both with/without film resistance in each case and they compared with experiment data showing good agreement. In the present study, we only compared with no film resistance case showing good agreement with their curves.

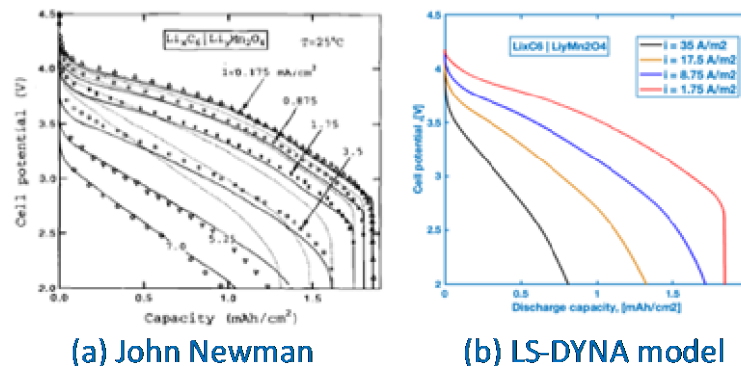


Figure 3 Validation of discharge capacity of the LMO based LIB model.

The coupling from the electrochemical solver to the thermal and mechanical solver is not easy process. It is mostly due to the different time scales among the solvers. Since the electric current flow is assumed to be in a steady-state, and the reaction on the boundary between the solid electrode and the electrolyte is extremely fast, therefore, in general, the time step in the battery solver is of the order of a second. By contrast, the mechanical time step is based on the Courant number, which is proportion to the time step divided by the speed of sound in the media and is of the order of the nanosecond to microsecond. To resolve the disparity of the time scales, we use a strategy of employing different schemes in the mechanical solver. For example, before the rigid ball impact on the battery stack, the implicit scheme of the mechanical solver was activated and after the rigid ball contacts the cell stack, the mechanical solver is switched to the explicit scheme. It is noted that while running the implicit scheme, the battery and thermal solver were activated with a strong numerical coupling to each other. In this way, we can simulate and complete the three way couplings among the solvers. The mechanical properties of the LIB such as Yong's modulus and Poisson's ratio was averaged with weighting factor based on length scale of each layer [17]. Figure 4 shows the snapshot at times right after the rigid ball initially contacts the LIB cell stack. As can clearly

be seen, a hot spot develops at 6 second after the ball contacts the LIB cell stack, meaning that the temperature inside of LIB starts to increase.

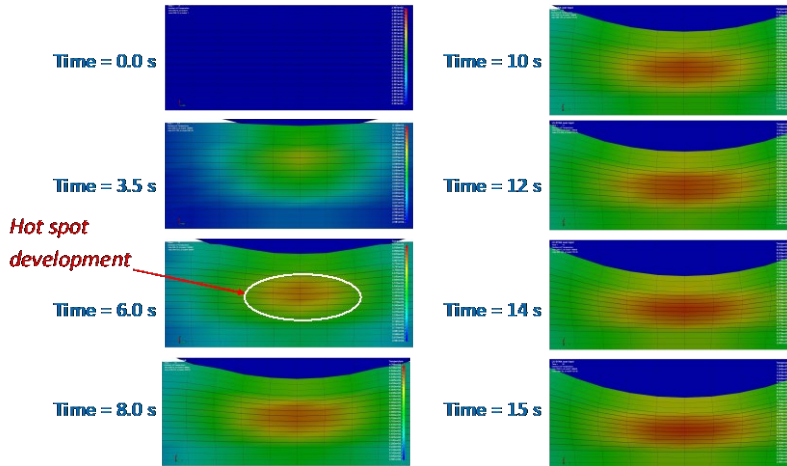
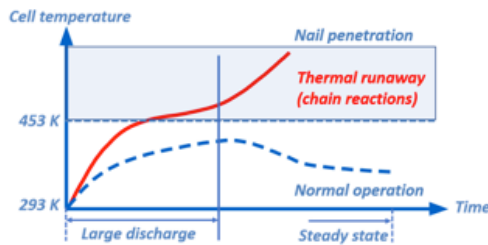
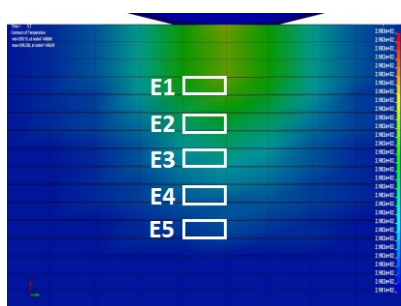


Figure 4 Time evolution snapshot after the ball impacted 10 cells of LIB stack.

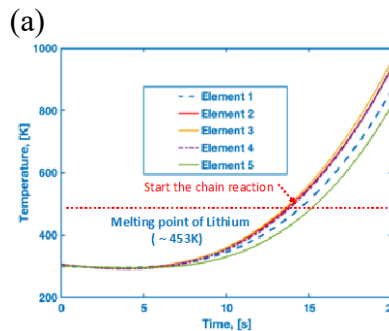
In case of a cell temperature increasing to a critical thresholding temperature like the melting point of the lithium, 453K at which stage the thermal runaway starts, and eventually a fire or explosion takes place, there is no way to control or suppress such a temperature increase as shown in Fig. 5(a) and (c).



$$\Delta T(x,t) = \frac{1}{H} \int_0^t q_{total}'' dt', \quad q_{total}'' = (\text{Joule} + \text{Peltier}) \text{ heating}$$



(b)



(c)

Figure 5 Analysis of the thermal runaways: (a) conceptual estimation of thermal runaway based on joule and Peltier heating modes, (b) individual cell elements inside battery cell stack, and (c) corresponding temperature increasing as function of time at each element.

During the deformation by impacting force, a cell’s temperature increases due to both Joule heating and Peltier heating, which is mostly due to an exothermal reaction initiated by the entropy changes inside of the battery cell. Figure 5(b) shows the individual cell elements inside LIB stack to monitor the temperature changes as function of time and Figure 5(c) shows the temperature increasing of each cell elements. As positioned in Figure 4, the rapid increasing of the temperature starts about 6s after the ball was in contact. After that point, temperatures in all elements increases exponentially to the thermal runaway. Although the present study is not modelling any

chemical reaction mechanism, it is speculated that the chain reactions could be started after reaching the melting point of the lithium metal at 453 K.

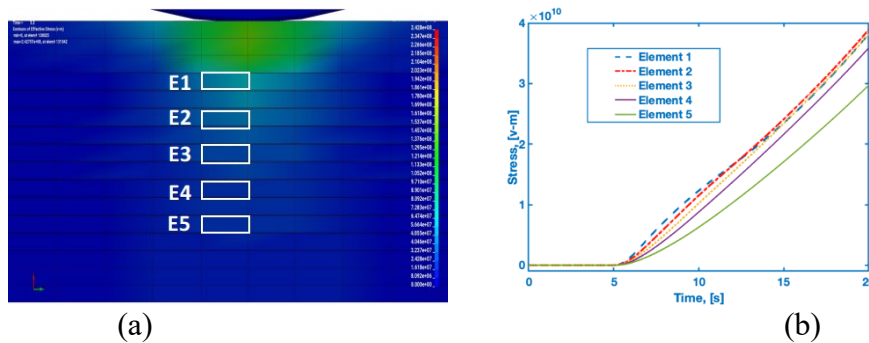


Figure 6 Stress analysis inside battery stack induced by impacting ball: (a) individual cell elements inside cell stack, and (b) corresponding Von Mises stress responses as a function of time at each element.

Figure 6 (a) and (b) show the individual elements of interesting and the corresponding changes of their Von Mises stress. Similarly, although much of stress is loaded on the steel case of LIB (not shown in Figure 6), the phenomena of battery cell stress increasing has the same trends as the temperature increasing in Fig. 5. More detailed studies on the relation between stress and temperature could be a topic for the future research and is beyond the scope of the present study.

Summary

In this presentation, we report a new development of the electrochemical-thermal-mechanical coupling based on previously developed electrochemical LIB model in LS-DYNA. In 10 cells of a lithium ion battery stack, each cell consists of Graphite(LiC_6) anode/Separator/high performance layered LMO(LiMn_2O_4) cathode, which has been strongly proposed as a candidate for automotive batteries because of its high capacity, thermal stability, and low volume change rate (cycle performance). For the thermal-mechanical analysis, each layer in a cell and outside cases are modeled corresponding to their material properties. Then, a rigid ball impacts the center top position of the cell stack in order to investigate the thermal and mechanical responses of a lithium ion battery stack. To see the cell responses inside LIB, we selected the first 20 seconds of the time period during the initial discharging process of the battery operation. The results show that a hot spot was developed in a few seconds of deformation and the rapid temperature increase over the melting point of the lithium was detected, where the thermal runaway eventually takes place. In addition, with the present development of the battery-thermal-mechanical interaction, we strongly believe that users can apply this to more complex applications such as a cellular phone deformation and even EV battery deformation test in automotive industries.

References

- [1] D. Linden and T. B. Reddy. Handbook of Batteries. McGraw-Hill Companies, Inc., New York, 3rd edition, 2002.
- [2] C. Mikolajczak, M. Kahn, K. White, and R. T. Long. Lithium-Ion Batteries Hazard and Use Assessment. Technical Report July, Exponent Failure Analysis Associates, Inc., 2011.
- [3] Y. Xia, T. Wierzbicki, E. Sahraei, X. Zhang, J. Power Sources 267 78-97, 2014.
- [4] Y. Chen and J. W. Evans, J. Electrochem. Soc., 140, 1833, 1993.
- [5] Y. Chen and J. W. Evans, J. Electrochem. Soc., 141, 2947, 1994.
- [6] C. R. Pal and J. Newman, J. Electrochem. Soc., 142, 3282, 1995.
- [7] Li Song and J. W. Evans, J. Electrochem. Soc., 147, 2086, 2000.
- [8] M. Doyle, T.F. Fuller, and J. Newman, J. Electrochem. Soc., 140, 1526, 1993.
- [9] T.F. Fuller, M. Doyle, and J. Newman, J. Electrochem. Soc., 141, 1, 1994.
- [10] E. J. Cheng, N. J. Taylor, J. Wolfenstine, J. Sakamoto, J. Asian Ceramic Societies, 5, 113, 2017.

-
- [11] J. Newman and W. Tiedmann, *AICHE J.*, 21. 25, 1975
- [12] R. B. Bird, W.E. Stewart, and E.N. Lightfoot, “*Transport Phenomena*” John Wiley and Sons, Inc. New York, 1960.
- [13] L. Onsager, *Annals New York Acad. Science*, 46, 242,1945.
- [14] J. Newman and Karen E. Thomas-Alyea, “*Electrochemical Systems*”, 3rd Edition, John Wiley and Sons, Inc. New Jersey, (2004).
- [15] 2020 LS-DYNA Multi-Physics Theory Manual at www.lstc.com.
- [16] L. Rao and J. Newman, *J. Electrochem. Soc.*, 144, 2697, 1997.
- [17] M. Doyle, J. Newman, A. S. Gozdz, C. N. Schmutz, and J.-M. Tarascon, *J. Electrochem. Soc.*, Vol 143, No 6 1890, 1996.